MATERIALS SCIENCE

Small-molecule organic ice microfibers

Bowen Cui[1], Peizhen Xu[1], Kailong Fan[1], Yuqi Zhen[1], Xiangzheng Li[1], Rusi Lu[1], Pan Wang[1,2], Xin Guo[1,2]*, Limin Tong[1,3]*

Small organic molecules are essential building blocks of our universe, from cosmic dust to planetary surfaces to life. Compared to their well-known gaseous and liquid forms that have been extensively studied, small organic molecules in the form of ice at low temperatures receive much less attention. Here, we show that supercooled small-molecule droplets can be drawn into highly uniform amorphous ice microfibers with lengths up to 5 cm and diameters down to 200 nm. In the experimental test, these fiber-like ices manifest excellent mechanical flexibilities with elastic strain up to 3.3%. Meanwhile, they can guide light with loss down to 0.025 dB/cm that approaches the material absorption limit and offer high optical nonlinearity for low-threshold supercontinuum generation. Notable temperature-dependent Young's modulus and icing-induced refractive-index increase are also found. These results may open a promising category of low-temperature materials for both scientific research and technological applications.

INTRODUCTION

Small organic molecules, primarily composed of the most abundant elements including carbon, hydrogen, and oxygen in the universe (*1*), have well-defined chemical structures and molecular weights. Compared with inorganic materials, these molecules generally exhibit superior multifunctionality, designability, tailorability, and hospitability and are irreplaceable in broad areas ranging from condensed matter physics, organic chemistry, materials science, biology, life science, to astronomy and space exploration (*2*–*6*). Besides their gaseous or liquid state typically found on the Earth, small-molecule organic compounds in the form of ice exist ubiquitously in extreme interstellar environments as substantial components of cosmic dust, interstellar clouds, and planetary surfaces (*7*–*9*) and play essential roles in soft matter physics, disordered solid systems, planetary geology, and astrochemistry (*10*–*12*). In the past decades, studies on organic ices have focused on spectra features (*13*, *14*), phase transition (*15*, *16*), and photochemical processes (*17*, *18*). However, their ultimate mechanical and optical properties that are critical for better understanding their intrinsic behaviors, as well as for releasing their full potentials for functional applications, have yet to be explored.

As a versatile platform for exploring ultimate physical (e.g., optical and mechanical) and chemical (e.g., catalytic) properties of materials, one-dimensional microfibers or nanowires have been attracting particular interest in recent years (*19*–*24*). Owing to their excellent structural integrity, small transverse dimension, and low defect density, these structures have been widely used for investigating ultimate mechanical and optical properties of materials ranging from carbon (*25*, *26*), semiconductor (*21*, *27*), silica glass (*19*, *28*), to water ice (*29*, *30*). Compared to their bulk counterparts which usually contain a certain amount of structural defects and geometric irregularities, these highly uniform one-dimensional structures can manifest much better physical properties [e.g., mechanical strength (*26*, *29*) and optical loss (*19*, *29*, *31*)].

Here, we succeeded in drawing amorphous ice microfibers (IMFs) directly from small-molecule organic droplets during vitrification at cryogenic temperatures, with diameters ranging from 200 nm to 10 μm and lengths up to 5 cm. We show that these small-molecule amorphous organic IMFs (OIMFs), with smooth surfaces and uniform diameters, can manifest favorable physical properties including high mechanical elasticity, low waveguiding loss, and high optical nonlinearity.

RESULTS

Fabrication and morphology of OIMFs

The OIMFs are fabricated by drawing supercooled viscous organic droplets around their glass transition temperatures (T_g), as shown schematically in Fig. 1 (A and B). For example, for ethanol IMFs, we firstly dropped an ethanol droplet (hundreds of picoliters in volume) into a gap of tens of micrometers between two end-cleaved and aligned silica fibers (SMF-28e, Corning Inc.) with diameter of 125 μm at room temperature (Fig. 1A), cooled down the gap area to a temperature slightly higher than T_g [i.e., ~110 K for ethanol with T_g of 97 K (*32*)] within a few seconds, and transformed the ethanol droplet into a viscous state. We then pulled the two fibers (by precise motor stages) apart bidirectionally with a velocity of 0.4 mm/s (Fig. 1B and movie S1), forming an ethanol IMF between the two silica fibers. By using this method, almost all vitrifiable organic liquids (e.g., methanol, toluene, ethylbenzene, ethylene glycol, and glycerol) can be drawn into IMFs with diameters ranging from 10 μm to 200 nm and lengths up to 5 cm (fig. S1). Figure 1C shows an optical micrograph of a 10-mm–length ethanol IMF with a waist diameter of 2.8 μm at the central area. Despite of the biconical profile of the OIMF as a whole, the 0.3-mm–length OIMF shown here is highly uniform in diameter. For higher-resolution characterization, we used a cryo-transmission electron microscope (cryo-TEM) working at 83 K to investigate the morphology and crystalline structure of these OIMFs (fig. S2). Figure 1D shows a typical cryo-TEM image of a benzyl acetate IMF (T_g of ~220 K) with a diameter of 880 nm. The excellent diameter uniformity and smooth surface are clearly seen. Figure 1E gives a close-up examination of the surface of the OIMF,

[1]New Cornerstone Science Laboratory, State Key Laboratory of Extreme Photonics and Instrumentation, College of Optical Science and Engineering, Zhejiang University, Hangzhou 310027, China. [2]Jiaxing Key Laboratory of Photonic Sensing & Intelligent Imaging, Intelligent Optics & Photonics Research Center, Jiaxing Research Institute Zhejiang University, Jiaxing 314000, China. [3]Collaborative Innovation Center of Extreme Optics, Shanxi University, Taiyuan 030006, China.
*Corresponding author. Email: guoxin@zju.edu.cn (X.G.); phytong@zju.edu.cn (L.T.)

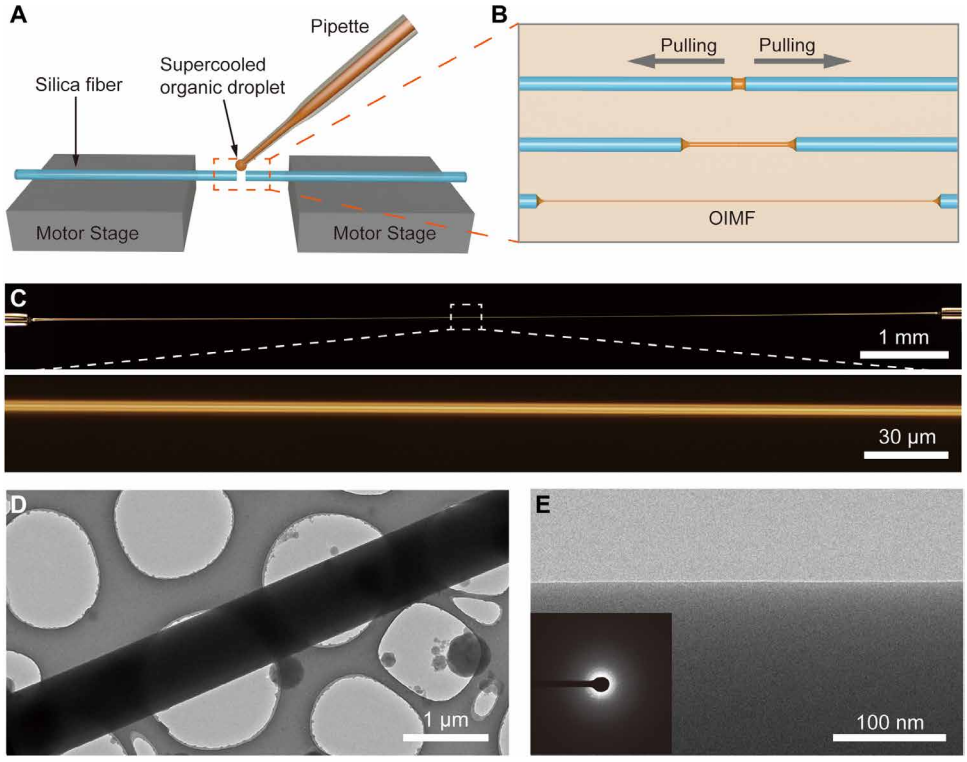

Fig. 1. Fabrication and microscopic characterization of small-molecule OIMFs. (**A** and **B**) Schematic diagrams of the experimental setup (A) and drawing processes (B) for OIMFs. (**C**) (top) Optical microscopic image of a 10-mm-length ethanol IMF with two ends connected to silica fibers. (bottom) Close-up optical microscopic image of the boxed section of the fiber with a uniform waist diameter of 2.8 μm. (**D**) A cryo-TEM image of an 880-nm–diameter benzyl acetate IMF. (**E**) Close-up cryo-TEM image of the surface of the benzyl acetate IMF in (D). Inset, electron diffraction pattern demonstrating the amorphous structure of the OIMF.

with a measured root mean square roughness of about 0.5 nm (see also fig. S3). The electron diffraction pattern (Fig. 1E, inset) confirms that the OIMF is amorphous, agreeing with the feature structure of the glass state (*19*, *33*).

Mechanical behavior of small-molecule OIMFs

Because of the low defect density and high structural uniformity, as-drawn OIMFs manifest high flexibility (e.g., stretching and bending) and excellent mechanical properties. For quantitative tensile tests, we used ethylene glycol IMFs with diameters ranging from 680 nm to ~10 μm as typical examples. The as-drawn OIMF was naturally connected to the ends of two silica fibers, which were respectively mounted on a high-precision translation stage (Q-521, PI Inc.) and a force sensor (NFS-C, Nators Inc.) (upper panel, Fig. 2A). The test was performed by stretching the OIMF with a velocity of 5 μm/s, with corresponding strain rates ranging from 0.002 to 0.02 s^{-1} at different temperatures. The real-time elongation was measured by relative displacement of two random water ice particles on the OIMF surface (lower panel, Fig. 2A), and the tensile force was obtained by the force sensor. During the test, the low environmental temperature was maintained in an isolated cryo-chamber filled with vaporized liquid nitrogen for long-time operation (fig. S4). Figure 2B gives typical engineering stress-strain curves of multicycle loading-unloading test on a 7.5-μm–diameter ethylene glycol IMF at 98 K, demonstrating a nearly linear elastic response with a strain up to 3.3%. When the temperature rises from 103 to 133 K, the OIMF undergoes a transition from brittleness to ductility (Fig. 2C) due to the gradual dominance of viscous deformation at higher temperatures (fig. S5 and movie S2), leading to a reduced yield strength (Fig. 2D) (*34*–*36*). By fitting the slope of stress-strain curves within the linear region, we obtain temperature-dependent Young's modulus, which decreases with increasing temperatures (Fig. 2D). Unlike the trend often seen in many other nanofibers (*37*, *38*), no obvious dependence of Young's modulus on the diameter is observed (figs. S6 and S7), because of the insufficient surface effect in OIMFs with relatively larger diameters.

Optical characterization of small-molecule OIMFs

The excellent diameter uniformity and surface smoothness allow OIMFs to serve as low-loss optical waveguides at low temperatures. The probing light was coupled into and out of an as-drawn OIMF through the taper region connected with standard silica fibers at both ends (figs. S8 and S9). When the light was guided through the OIMF and coupled back to the silica fiber at the other end, the scattering of the joint at the output end of the OIMF (Fig. 3A) was much stronger than that of sidewall along its length, indicating the low waveguiding loss of the OIMF. The loss of the OIMF increases with decreasing diameter and increasing wavelength (fig. S10), similar to those observed in typical glass micro/nanofibers (*19*, *39*, *40*). Figure 3B shows an evolution of transmission intensity at 980 nm wavelength in an ethylbenzene IMF drawing process (see also movie S3), during which high-order modes keep vanishing (indicated by the abrupt drops of transmittance) until only the fundamental mode (HE_{11}) remains, a typical waveguiding behavior in an optical microfiber

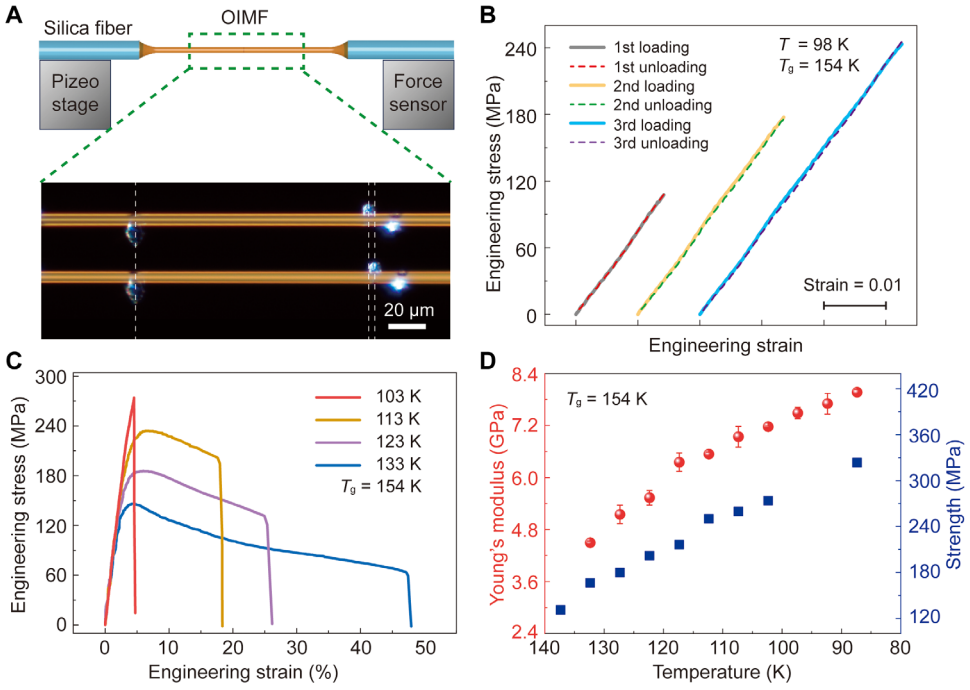

Fig. 2. Mechanical characterization of small-molecule OIMFs. (**A**) Schematic diagram of the experimental setup (upper) and optical microscopic images of an ethylene glycol IMF before and after axial force loading (lower). The vertical white dashed lines indicate the elongation of the OIMF before and after stretching. (**B**) Engineering stress-strain curves of a 7.5-μm–diameter ethylene glycol IMF for multicycle loading-unloading tests. (**C**) Temperature-dependent stress-strain curves of ethylene glycol IMFs with diameters around 8 μm. (**D**) Temperature-dependent strength and Young's modulus of ethylene glycol IMFs with diameters from 680 nm to ~10 μm.

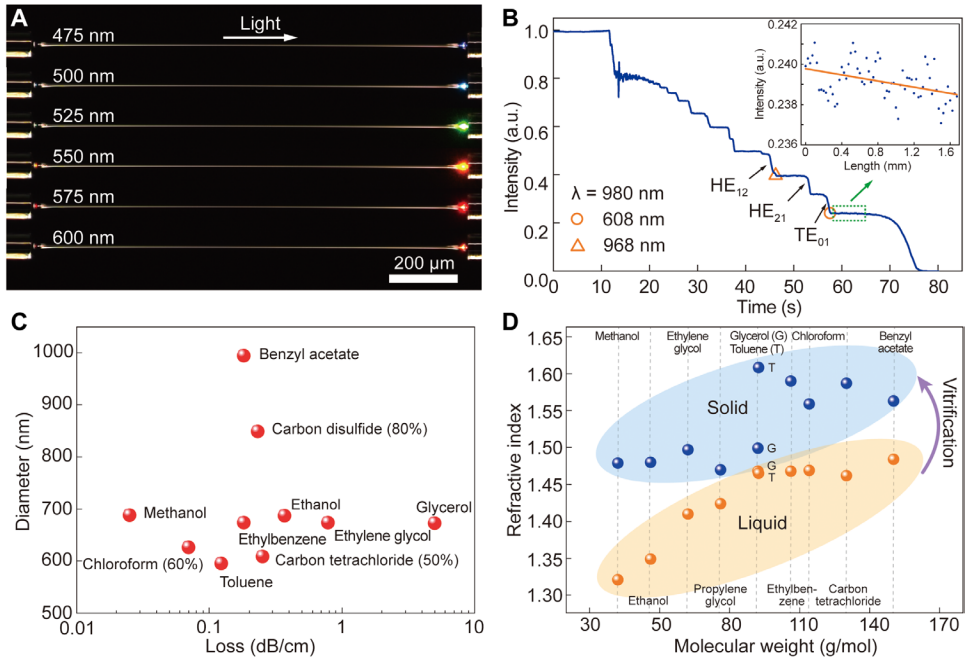

Fig. 3. Optical characterization of small-molecule OIMFs. (**A**) Optical microscopic images of a 1.3-μm–diameter, 1.2-mm–length ethanol IMF guiding light with different wavelengths. The white arrow depicts the direction of light propagation. (**B**) Real-time transmission measurement at 980 nm wavelength during the drawing process of an ethylbenzene IMF. Inset, length-dependent output intensity of the fundamental mode (HE_{11}) indicated by the green dotted box. (**C**) Measured propagation losses of typical OIMFs with different diameters at 980 nm wavelength. (**D**) Refractive indices of typical organic ices near T_g and their corresponding liquids at room temperature.

during its taper drawing process (*41*, *42*). By calculating the cutoff diameter of a specific high-order mode, the diameters of the as-drawn OIMFs can be determined with high accuracy and precision (*41*–*43*). For example, the modes HE_{12} and TE_{01} cut off at 968 and 608 nm diameters, respectively (fig. S11). From the length-dependent transmittivity of the ethylbenzene IMF (inset of Fig. 3B), a waveguide loss of ~0.2 dB/cm at 980 nm wavelength can be obtained for the fundamental mode (HE_{11}). Similarly, we have measured waveguiding losses of a variety of OIMFs (Fig. 3C), with the lowest loss of 0.025 dB/cm in a 690-nm–diameter methanol IMF. Notably, the measured losses of several OIMFs, including toluene, ethanol, and ethylene glycol IMFs, are approaching their intrinsic material absorption (fig. S12), indicating the negligible scattering loss of a high-uniformity OIMF.

For optical applications, the refractive index of the material is one of the most important parameters. However, so far precise refractive indices of these amorphous organic ices are mostly lacking. Here, by using a dual-fiber Fabry-Pérot (FP) cavity setup (see Materials and Methods and fig. S13), we precisely measured the refractive indices of these amorphous organic ices for the first time (table S1). As shown in Fig. 3D, the measured refractive indices of ices at a temperature slightly lower than T_g have higher values than their corresponding liquids, showing an evident icing-induced refractive-index increase. Also, the refractive indices increase basically with the molecular weights of the amorphous ices (Fig. 3D).

Functional applications of small-molecule OIMFs

Benefitting from their high mechanical flexibilities and low optical losses, these OIMFs can be readily adopted for functional applications at low temperature. Figure 4A shows assembling a long free-standing 1.5-μm–diameter ethanol IMF into a closed microloop with a minimum diameter of 92 μm by micromanipulation under an optical microscope (*44*) (see also movie S4). At the temperature of 88 K, the loop can be elastically assembled and released repeatedly with a maximum elastic strain of 1.6%, no plastic deformation was noticed. When a white light was coupled in and transmitted through a 160-μm–diameter loop (inset of Fig. 4B), broadband optical resonances were observed (Fig. 4B) with a free spectral range (FSR) of 0.87 nm around 826 nm wavelength (Fig. 4C), agreeing well with the calculated value of 0.92 nm in the 160-μm–diameter loop resonator (*45*).

Compared with typical inorganic materials with relatively small molecular weights used for optical micro/nanofibers [e.g., silica (*46*)]

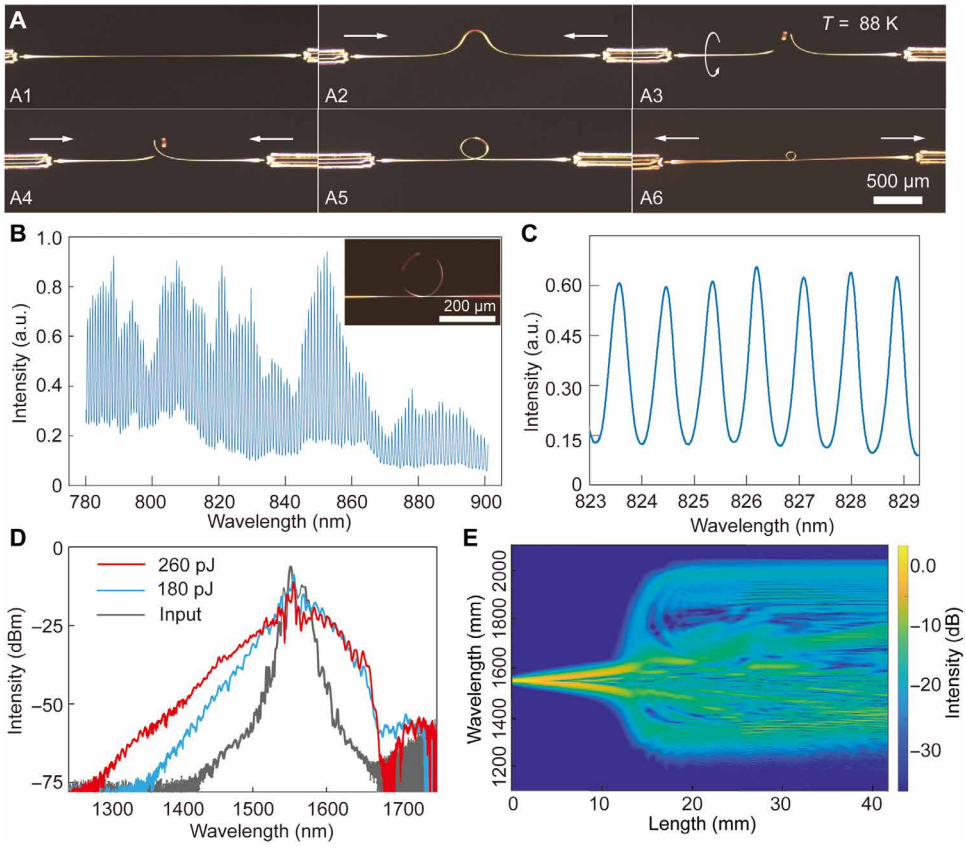

Fig. 4. Functional applications of small-molecule OIMFs. (**A**) Optical microscopic images illustrating the assembly of a free-standing ethanol IMF into a microloop resonator. Steps: [(A1) to (A2)], Bend the OIMF by moving the two silica fibers towards each other; [(A3) to (A4)], flip the bent OIMF by twisting a silica fiber, and adjust the silica fibers to assemble the OIMF into a closed loop; and (A5) to (A6)], tighten the OIMF to modulate the diameter of the microloop. (**B**) Typical transmission spectrum from 780 to 900 nm wavelength of an ethanol IMF microloop with a diameter of 160 μm. Inset, optical microscopic image of the OIMF microloop resonator. (**C**) Close-up view of the transmission spectrum from 823 to 829 nm wavelength, with a measured FSR of 0.87 nm. (**D**) Supercontinuum spectra generated from a ~20-mm–length carbon tetrachloride-ethylbenzene (50:50) IMFs, pumped by 200-fs laser pulses with 1550 nm wavelength from an 86-MHz Er-doped fiber laser. (**E**) Simulated spectral evolution of 200-fs pulses with 1550 nm wavelength and 260 pJ input energy in a 1.1-μm–diameter carbon tetrachloride-ethylbenzene (50:50) IMF.

or supercontinuum generation [e.g., water (*47*)], the organic small-molecule ices have much higher (e.g., more than one order of magnitude) optical nonlinearity (table S2). Also, compared to their bulk counterparts, the OIMFs with subwavelength diameters can offer strong optical confinement along much larger light-material interaction lengths (*43*), which can further enhance the effective nonlinear coefficient of a waveguiding OIMF (*48*), and will thus be favorable for low-threshold optical nonlinear applications. As an example, here we used a 1.1-μm–diameter, ~20-mm–length carbon tetrachloride-ethylbenzene (50:50) IMF for supercontinuum generation. When 1550-nm-wavelength, 200-fs laser pulses from an 86-MHz Er-doped fiber laser (MERCURY 1550-100-PM, Polaronyx Inc.) were coupled into and propagated through the OIMF, notable spectral broadening was observed when the input pulse energy exceeded 180 pJ, and a supercontinuum from 1300 to 1800 nm wavelength was generated when the input pulse energy reached 260 pJ (Fig. 4D), agreeing roughly with theoretical calculations (Fig. 4E, see also Materials and Methods). The slight difference in spectrum may come from the uncertainties in the diameter of OIMFs, input pulse wavelength and duration (*49*).

DISCUSSION

So far, we have fabricated high-quality amorphous OIMFs by drawing supercooled small-molecule droplets. These fiber-like amorphous ices, with lengths up to 5 cm and diameters from several micrometers to 200 nm, manifest excellent mechanical and optical properties for using as promising functional materials at cryogenic environments. For example, the high mechanical elasticity and flexibility, incorporated with its high aspect ratio and one-dimensional geometry, may enable its use for microrings and springs at low temperature, as well as for cryogenic bonding and bridging at microscale. Meanwhile, the low loss for linear optical waveguiding and high nonlinearity for optical modulation and frequency conversion may open opportunities in advancing nanophotonics for low-temperature applications. Last, the successful fabrication of these highly uniform low-dimensional amorphous ices, as well as the experimental capability of revealing their intrinsic physical properties, may suggest a versatile platform for exploring an unexplored category of ice functional materials that appear as gases or liquids at room temperature but solids at low temperature.

MATERIALS AND METHODS

Measurement of refractive indices of glassy organic ices

To precisely determine refractive indices of organic ices, we used a dual fiber FP cavity system (fig. S13, A and B) to reduce system errors resulting from the cavity length variation. The system includes a tunable continuous-wave laser (TSL-710, 1480 to 1640 nm, Santec Inc.), a power meter (MPM-210H, Santec Inc.) and three 50:50 couplers. The two fiber FP cavities (reference cavity FP1 and measurement cavity FP2) are created by two end-cleaved and aligned silica fibers and fixed on the same stage. To enhance the reflectivity, gold films with a thickness of ~20 nm are deposited on the fiber ends using magnetron sputtering. Reflectance spectra are recorded and the FSRs of the fiber FPs before ($\Delta\lambda_1$, $\Delta\lambda_2$) and after ($\Delta\lambda_1'$, $\Delta\lambda_2'$) adding the amorphous organic ice are obtained, satisfying the following equations (*50*)

$$\begin{cases} \dfrac{\Delta\lambda_1}{\Delta\lambda_1'} = \dfrac{L_1+\Delta L}{L_1} \\ \dfrac{\Delta\lambda_2}{\Delta\lambda_2'} = \dfrac{L_2+\Delta L}{L_2}\dfrac{n}{n_{\text{air}}} \\ \dfrac{\Delta\lambda_2}{\Delta\lambda_1} = \dfrac{L_1}{L_2} \end{cases} \tag{1}$$

where L_1 and L_2 are the original lengths of FP1 and FP2, respectively, n and n_{air} are the refractive indices of the organic ice and air (here $n_{\text{air}} = 1$), and ΔL is the length change of the stage during the cooling process of organic liquids. From Eq. 1, we are able to obtain the refractive index of the organic ice (n) by

$$\frac{n_{\text{air}}}{n} = \left[1+\Delta\lambda_2\left(\frac{1}{\Delta\lambda_1'}-\frac{1}{\Delta\lambda_1}\right)\right]\frac{\Delta\lambda_2'}{\Delta\lambda_2} \tag{2}$$

For example, from the reflectance spectra (fig. S11C) collected for toluene at 106 K ($\Delta\lambda_1 = 5.38$ nm, $\Delta\lambda_1' = 5.35$ nm, $\Delta\lambda_2 = 11.10$ nm, and $\Delta\lambda_2' = 6.80$ nm), we can obtain a refractive index of 1.61 according to Eq. 2.

Simulation of propagation of ultrashort laser pulses in OIMFs

We use the generalized nonlinear Schrödinger equation (*51*, *52*) to simulate the propagation of ultrashort laser pulses through the OIMFs

$$\frac{\partial A(z,t)}{\partial z} = i\sum_{k=2}^{k_{\max}}\frac{i^k}{k!}\beta_k\frac{\partial^k A(z,t)}{\partial t^k} + i\gamma\left(1+\frac{i}{\omega_0}\frac{\partial}{\partial t}\right)\left[A(z,t)\int_0^\infty R(t')\,|A(z,t-t')|^2\,dt'\right]$$

where $A(z,t)$ is the electric field envelope, k is the term of Taylor series, β_k is the dispersion coefficients at the pump frequency ω_0, and $\gamma = n_2\omega_0/cA_{\text{eff}}$ is the nonlinear coefficient, where $n_2 = 1.5\times10^{-19}\text{m}^2/\text{W}$ (*53*), A_{eff} is the effective mode area of the waveguided mode, and c is the speed of light in vacuum. The kernel $R(t')$ of the integral operator for nonlinear response of the medium is taken from experiments (*54*). We simulated the propagation of 200-fs laser pulses at 1550 nm wavelength in a 1.1-μm-diameter OIMF, revealing a nonlinear spectral broadening at an input pump energy of 260 pJ. The physical parameters of the OIMF are summarized in Table 1.

Table 1. Dispersion coefficients and effective mode area in a 1.1-μm-diameter OIMF at 1550-nm wavelength.

λ (nm)	β_2 (s^2/m)	β_3 (s^3/m)	β_4 (s^4/m)	β_5 (s^5/m)	A_{eff} (μm^2)
1550	-1.16×10^{-25}	-2.49×10^{-39}	2.11×10^{-53}	-1.44×10^{-67}	0.9

Supplementary Materials

The PDF file includes:

Figs. S1 to S13
Tables S1 and S2
Legends for movies S1 to S4
References

Other Supplementary Material for this manuscript includes the following:

Movies S1 to S4

REFERENCES AND NOTES

1. H. E. Suess, H. C. Urey, Abundances of the elements. *Rev. Mod. Phys.* **28**, 53–74 (1956).
2. P. G. Debenedetti, F. H. Stillinger, Supercooled liquids and the glass transition. *Nature* **410**, 259–267 (2001).
3. S. A. Kivelson, G. Tarjus, In search of a theory of supercooled liquids. *Nat. Mater.* **7**, 831–833 (2008).
4. Y. Wang, S.-Y. Ran, B. Man, G. Yang, Ethanol induces condensation of single DNA molecules. *Soft Matter* **7**, 4425–4434 (2011).
5. A. C. A. Boogert, P. A. Gerakines, D. C. B. Whittet, Observations of the icy universe. *Annu. Rev. Astron. Astrophys.* **53**, 541–581 (2015).
6. P. Zhang, H. Du, S. Cui, P. Zhou, Y. Xu, Response of organic solvents to vitrification and electron exposure in cryo-TEM experiments. *Respons. Mater.* **1**, e20230025 (2023).
7. R. D. Lorenz, K. L. Mitchell, R. L. Kirk, A. G. Hayes, O. Aharonson, H. A. Zebker, P. Paillou, J. Radebaugh, J. I. Lunine, M. A. Janssen, S. D. Wall, R. M. Lopes, B. Stiles, S. Ostro, G. Mitri, E. R. Stofan, Titan's inventory of organic surface materials. *Geophys. Res. Lett.* **35**, L02206 (2008).
8. K. I. Öberg, A. C. A. Boogert, K. M. Pontoppidan, S. van den Broek, E. F. van Dishoeck, S. Bottinelli, G. A. Blake, N. J. Evans II, The *Spitzer* ice legacy: Ice evolution from cores to protostars. *Astrophys. J.* **740**, 109 (2011).
9. S. Kwok, Amorphous organic solids as a component of interstellar dust. *Earth Planet Space* **63**, 1021–1026 (2011).
10. K. I. Öberg, Photochemistry and astrochemistry: Photochemical pathways to interstellar complex organic molecules. *Chem. Rev.* **116**, 9631–9663 (2016).
11. W. Zhang, X. Zhang, B. W. Edwards, L. Zhong, H. Gao, M. J. Malaska, R. Hodyss, J. R. Greer, Deformation characteristics of solid-state benzene as a step towards understanding planetary geology. *Nat. Commun.* **13**, 7949 (2022).
12. A. Zaccone, *Theory of Disordered Solids* (Springer International Publishing, 2023).
13. R. G. Urso, D. Baklouti, Z. Djouadi, N. Pinilla-Alonso, R. Brunetto, Near-infrared methanol bands probe energetic processing of icy outer solar system objects. *Astrophys. J.* **894**, L3 (2020).
14. M. Guélin, J. Cernicharo, Organic molecules in interstellar space: Latest advances. *Front. Astron. Space Sci.* **9**, 787567 (2022).
15. B. H. Torrie, O. S. Binbrek, M. Strauss, I. P. Swainson, Phase transitions in solid methanol. *J. Solid State Chem.* **166**, 415–420 (2002).
16. L. Ciabini, F. A. Gorelli, M. Santoro, R. Bini, V. Schettino, M. Mezouar, High-pressure and high-temperature equation of state and phase diagram of solid benzene. *Phys. Rev. B* **72**, 094108 (2005).
17. G. M. Muñoz Caro, U. Meierhenrich, W. A. Schutte, W. H.-P. Thiemann, J. M. Greenberg, UV-photoprocessing of interstellar ice analogs: Detection of hexamethylenetetramine-based species. *Astron. Astrophys.* **413**, 209–216 (2004).
18. J. H. Waite, D. T. Young, T. E. Cravens, A. J. Coates, F. J. Crary, B. Magee, J. Westlake, The process of tholin formation in Titan's upper atmosphere. *Science* **316**, 870–875 (2007).
19. L. Tong, R. R. Gattass, J. B. Ashcom, S. He, J. Lou, M. Shen, I. Maxwell, E. Mazur, Subwavelength-diameter silica wires for low-loss optical wave guiding. *Nature* **426**, 816–819 (2003).
20. Y. Xia, P. Yang, Y. Sun, Y. Wu, B. Mayers, B. Gates, Y. Yin, F. Kim, H. Yan, One-dimensional nanostructures: Synthesis, characterization, and applications. *Adv. Mater.* **15**, 353–389 (2003).
21. R. Yan, D. Gargas, P. Yang, Nanowire photonics. *Nat. Photonics* **3**, 569–576 (2009).
22. P. Wang, Y. Wang, L. Tong, Functionalized polymer nanofibers: A versatile platform for manipulating light at the nanoscale. *Light Sci. Appl.* **2**, e102 (2013).
23. L. Bu, S. Guo, X. Zhang, X. Shen, D. Su, G. Lu, X. Zhu, J. Yao, J. Guo, X. Huang, Surface engineering of hierarchical platinum-cobalt nanowires for efficient electrocatalysis. *Nat. Commun.* **7**, 11850 (2016).
24. J. Zhang, H. Fang, P. Wang, W. Fang, L. Zhang, X. Guo, L. Tong, Optical microfiber or nanofiber: A miniature fiber-optic platform for nanophotonics. *Photon. Insights* **3**, R02 (2024).
25. M.-F. Yu, O. Lourie, M. J. Dyer, K. Moloni, T. F. Kelly, R. S. Ruoff, Strength and breaking mechanism of multiwalled carbon nanotubes under tensile load. *Science* **287**, 637–640 (2000).
26. A. Banerjee, D. Bernoulli, H. Zhang, M.-F. Yuen, J. Liu, J. Dong, F. Ding, J. Lu, M. Dao, W. Zhang, Y. Lu, S. Suresh, Ultralarge elastic deformation of nanoscale diamond. *Science* **360**, 300–302 (2018).
27. L. T. Ngo, D. Almécija, J. E. Sader, B. Daly, N. Petkov, J. D. Holmes, D. Erts, J. J. Boland, Ultimate-strength germanium nanowires. *Nano Lett.* **6**, 2964–2968 (2006).
28. G. Brambilla, D. N. Payne, The ultimate strength of glass silica nanowires. *Nano Lett.* **9**, 831–835 (2009).
29. P. Xu, B. Cui, Y. Bu, H. Wang, X. Guo, P. Wang, Y. R. Shen, L. Tong, Elastic ice microfibers. *Science* **373**, 187–192 (2021).
30. B. Cui, P. Xu, X. Li, K. Fan, X. Guo, L. Tong, Low-dimensional and confined ice. *Annu. Rev. Mat. Res.* **53**, 371–397 (2023).
31. J. E. Hoffman, S. Ravets, J. A. Grover, P. Solano, P. R. Kordell, J. D. Wong-Campos, L. A. Orozco, S. L. Rolston, Ultrahigh transmission optical nanofibers. *AIP Adv.* **4**, 067124 (2014).
32. C. A. Angell, J. M. Sare, E. J. Sare, Glass transition temperatures for simple molecular liquids and their binary solutions. *J. Phys. Chem.* **82**, 2622–2629 (1978).
33. B. K. Vainshtein, *Structure Analysis by Electron Diffraction* (Elsevier, 2013).
34. J. B. Wachtman Jr., W. E. Tefft, D. G. Lam Jr., C. S. Apstein, Exponential temperature dependence of Young's modulus for several oxides. *Phys. Rev.* **122**, 1754–1759 (1961).
35. C. Jiang, Z. Zhu, J. Zhang, Z. Yang, H. Jiang, Constitutive modeling of the rate- and temperature-dependent macro-yield behavior of amorphous glassy polymers. *Int. J. Mech. Sci.* **179**, 105653 (2020).
36. E. E. Ferrero, A. B. Kolton, E. A. Jagla, Yielding of amorphous solids at finite temperatures. *Phys. Rev. Mater.* **5**, 115602 (2021).
37. Y. Yang, Y. Cui, Z. Fu, T. Li, F. Xu, Y. Wang, Size-dependent mechanical behavior of a-silicon carbide nanowires under *in-situ* transmission electron microscopy tensile tests. *Mater. Res. Express* **6**, 045009 (2019).
38. K. Peng, A. Nain, R. Mirzaeifar, Tracking the origins of size dependency in the mechanical properties of polymeric nanofibers at the atomistic scale. *Polymer* **175**, 118–128 (2019).
39. G. Brambilla, V. Finazzi, D. J. Richardson, Ultra-low-loss optical fiber nanotapers. *Opt. Express* **12**, 2258–2263 (2004).
40. Y. Jung, G. Brambilla, D. J. Richardson, Broadband single-mode operation of standard optical fibers by using a sub-wavelength optical wire filter. *Opt. Express* **16**, 14661–14667 (2008).
41. Y. Xu, W. Fang, L. Tong, Real-time control of micro/nanofiber waist diameter with ultrahigh accuracy and precision. *Opt. Express* **25**, 10434–10440 (2017).
42. Y. Kang, J. Gong, Y. Xu, N. Yao, W. Fang, X. Guo, L. Tong, Ultrahigh-precision diameter control of nanofiber using direct mode cutoff feedback. *IEEE Photonic Tech. Lett.* **32**, 219–222 (2020).
43. L. Tong, J. Lou, E. Mazur, Single-mode guiding properties of subwavelength-diameter silica and silicon wire waveguides. *Opt. Express* **12**, 1025–1035 (2004).
44. M. Sumetsky, Y. Dulashko, A. Hale, Fabrication and study of bent and coiled free silica nanowires: Self-coupling microloop optical interferometer. *Opt. Express* **12**, 3521–3531 (2004).
45. M. Sumetsky, Y. Dulashko, J. M. Fini, A. Hale, D. J. DiGiovanni, The microfiber loop resonator: Theory, experiment, and application. *J. Lightwave Technol.* **24**, 242–250 (2006).
46. R. R. Gattass, G. T. Svacha, L. Tong, E. Mazur, Supercontinuum generation in submicrometer diameter silica fibers. *Opt. Express* **14**, 9408–9414 (2006).
47. A. Bozolan, C. J. S. de Matos, C. M. B. Cordeiro, E. M. dos Santos, J. Travers, Supercontinuum generation in a water-core photonic crystal fiber. *Opt. Express* **16**, 9671–9676 (2008).
48. M. A. Foster, A. L. Gaeta, Ultra-low threshold supercontinuum generation in sub-wavelength waveguides. *Opt. Express* **12**, 3137–3143 (2004).
49. J. M. Dudley, G. Genty, S. Coen, Supercontinuum generation in photonic crystal fiber. *Rev. Mod. Phys.* **78**, 1135–1184 (2006).
50. H. Pfeifer, L. Ratschbacher, J. Gallego, C. Saavedra, A. Faßbender, A. von Haaren, W. Alt, S. Hofferberth, M. Köhl, S. Linden, D. Meschede, Achievements and perspectives of optical fiber Fabry–Pérot cavities. *Appl. Phys. B* **128**, 29 (2022).
51. G. P. Agrawal, *Nonlinear Fiber Optics* (Academic Press, 2006).
52. S. M. Kobtsev, S. V. Smirnov, Modelling of high-power supercontinuum generation in highly nonlinear, dispersion shifted fibers at CW pump. *Opt. Express* **13**, 6912–6918 (2005).
53. Q. H. Dinh, J. Pniewski, H. L. Van, A. Ramaniuk, V. C. Long, K. Borzycki, K. D. Xuan, M. Klimczak, R. Buczyński, Optimization of optical properties of photonic crystal fibers infiltrated with carbon tetrachloride for supercontinuum generation with subnanojoule femtosecond pulses. *Appl. Optics* **57**, 3738–3746 (2018).
54. P. Zhao, M. Reichert, T. R. Ensley, W. M. Shensky III, A. G. Mott, D. J. Hagan, E. W. Van Stryland, Nonlinear refraction dynamics of solvents and gases. *Proc. SPIE* **9731**, 97310F (2016).
55. M. R. Carpenter, D. B. Davies, A. J. Matheson, Measurement of the glass-transition temperature of simple liquids. *J. Chem. Phys.* **46**, 2451–2454 (1967).
56. S. Kedenburg, M. Vieweg, T. Gissibl, H. Giessen, Linear refractive index and absorption measurements of nonlinear optical liquids in the visible and near-infrared spectral region. *Opt. Mater. Express* **2**, 1588–1611 (2012).

57. T. P. Otanicar, P. E. Phelan, J. S. Golden, Optical properties of liquids for direct absorption solar thermal energy systems. *Sol. Energy* **83**, 969–977 (2009).
58. Z. W. Wilkes, S. Varma, Y.-H. Chen, H. M. Milchberg, T. G. Jones, A. Ting, Direct measurements of the nonlinear index of refraction of water at 815 and 407 nm using single-shot supercontinuum spectral interferometry. *Appl. Phys. Lett.* **94**, 211102 (2009).
59. S. Yu, X. Wu, Y. Wang, X. Guo, L. Tong, 2D materials for optical modulation: Challenges and opportunities. *Adv. Mater.* **29**, 1606128 (2017).
60. P. P. Ho, R. R. Alfano, Optical Kerr effect in liquids. *Phys. Rev. A* **20**, 2170–2187 (1979).
61. M. Vieweg, T. Gissibl, S. Pricking, B. T. Kuhlmey, D. C. Wu, B. J. Eggleton, H. Giessen, Ultrafast nonlinear optofluidics in selectively liquid-filled photonic crystal fibers. *Opt. Express* **18**, 25232–25240 (2010).

Acknowledgments: We thank L. Y. Wu in the Center of Cryo-Electron Microscopy (CCEM), Zhejiang University for the technical assistance on cryo-TEM; J. B. Zhang for the helpful discussion on the measurement of propagation loss; and K. Y. Liu for assistance on the refractive index measurement. **Funding:** This work was supported by the National Key Research and Development Program of China (2023YFB2806701), the New Cornerstone Science Foundation (NCI202216), the National Natural Science Foundation of China (62175213 and 92150302), the Zhejiang Provincial Natural Science Foundation of China (LRG25F050001), and the Fundamental Research Funds for the Zhejiang Provincial Universities (2023QZJH27).
Author contributions: L.T. conceived the study and co-supervised the project with X.G. B.C. designed the experiments, performed the measurements, and analyzed the data. B.C. and P.X. fabricated the OIMFs and performed the experiment for mechanical behaviors measurement; B.C. performed the experiment for propagation loss and supercontinuum generation and ran the simulation for the supercontinuum generation; B.C., K.F., and R.L. measured the refractive index; Y.Z. and P.W. helped perform magnetron sputtering to deposit gold film on fiber ends; and B.C. and X.L. did the characterization of micoloop resonators. L.T., X.G., and B.C. wrote the manuscript. All authors discussed the results and commented on the paper. **Competing interests:** The authors declare that they have no competing interests. **Data and materials availability:** All data needed to evaluate the conclusions in the paper are present in the paper and/or the Supplementary Materials.

Submitted 5 August 2024
Accepted 3 December 2024
Published 8 January 2025
10.1126/sciadv.ads2538